Particulate impurities in cell-based medicinal products traced by flow imaging microscopy combined with deep learning for image analysis

A.D. Grabarek[1,2], E. Senel[1], T. Menzen[1], K.H. Hoogendoorn[3], K. Pike-Overzet[3], A. Hawe[1], W. Jiskoot[1,2,*]

[1] Coriolis Pharma, Martinsried, Germany
[2] Leiden Academic Centre for Drug Research, Leiden University, The Netherlands
[3] Department of Clinical Pharmacy and Toxicology, Leiden University Medical Center, Leiden, The Netherlands

ARTICLE INFO

ABSTRACT

Cell-based medicinal products (CBMPs) are rapidly gaining importance in the treatment of life-threatening diseases. However, the analytical toolbox for characterization of CBMPs is limited. The aim of our study was to develop a method based on flow imaging microscopy (FIM) for the detection, quantification and characterization of subvisible particulate impurities in CBMPs. Image analysis was performed by using an image classification approach based on a convolutional neural network (CNN). Jurkat cells and Dynabeads were used in our study as a representation of cellular material and non-cellular particulate impurities, respectively. We demonstrate that FIM assisted with CNN is a powerful method for the detection and quantification of Dynabeads and cells with other process related impurities, such as cell agglomerates, cell-bead adducts and debris. By using CNN, we achieved a more than 50-fold lower misclassification rate compared with the use of output parameters from the FIM software. The limit of detection was ~15 000 beads/mL in the presence of ~500 000 cells/mL, making this approach suitable for the detection of these particulate impurities in CBMPs. In conclusion, CNN-assisted FIM is a powerful method for the detection and quantification of cells, Dynabeads and other subvisible process impurities potentially present in CBMPs.

Introduction

Technological advancements in the past decades have profoundly revolutionized the area of biotherapeutics [1]. Cell-based medicinal products (CBMPs), an important category of medicinal products based on cells or tissues, are rapidly gaining significance because they can serve as an effective cure for patients where no other treatment option is available. Examples of CBMPs include stem cells, (genetically modified) T cells and (antigen-loaded) dendritic cells [2]. More than a thousand clinical trials with CBMPs are completed or underway (as of January 2020, www.clinicaltrials.gov), and regulatory agencies are expecting an increasing number of market approvals in the coming years [3]. A recent breakthrough in this field was the approval of two genetically engineered T cells (chimeric antigen receptor [CAR] T cells) in the United States in 2017 and in Europe in 2018. Despite their clinical success, challenges with respect to manufacturing and quality control (QC) must be faced to make CBMPs commercially viable [4].

Manufacturing of CBMPs, such as the current generation of CAR T cells, is a much more complex and labor-intensive process compared with the production of classical protein-based biologics [2,5]. For instance, the production of CAR T cells involves collection of cells from the patient via leukapheresis, *ex vivo* transduction with a viral vector, encoding the CAR transgene, T-cell activation and expansion, formulation, fill and finish, storage and QC before intravenous infusion. Moreover, the manufacturing processes involve the addition of raw materials, such as media, vector, cytokines or antibody-coated magnetic beads. Some of the raw materials can diminish the safety of the final drug product and are considered as impurities. An example are monoclonal antibody-coupled magnetic beads, which must be removed from the process to acceptable levels and need to be measured as part of product QC testing [6].

Most CBMPs consist of a suspension of living cells with a size typically between 10 and 30 μm. Lymphocytes, including T cells, are generally smaller in diameter and can range from 7 to 18 μm in diameter [7]. Therefore, only large-pore filters ($\geq$70-μm pore size) can be used during manufacture. Such filtration is not capable of removing particulate impurities within the micron and submicron size range. Ineffective removal of these particulates, derived either from raw materials or from manufacturing processes, may potentially lead to adverse

* Correspondence: Wim Jiskoot, PhD, Division of BioTherapeutics, Leiden Academic Centre for Drug Research, Leiden University, Einsteinweg 55, 2333 CC Leiden, The Netherlands. Phone +31(0)715274314.

E-mail address: w.jiskoot@lacdr.leidenuniv.nl (W. Jiskoot).

reactions in patients [8]. Micrometer-sized extrinsic particles (e.g., glass particles, metal particles, fibers) may result in occlusion of small capillaries of the circulatory system [9]. Moreover, proteins can adsorb to such non-proteinaceous particles, which may result in unwanted immunogenicity [10]. Furthermore, micro- and submicron-sized proteinaceous particles, which may originate from cells or cell culture medium, have been shown to increase the risk of unwanted immunogenicity [11]. In addition, necrotic cells and cell debris tend to have a smaller diameter compared with healthy cells [12]. Therefore, monitoring the size of cells and other particulate matter may aid in assessing the quality of CBMPs.

For CBMPs, because of their particulate nature, it is challenging to fulfill specific pharmacopeial testing requirements. The compedial specifications set limits for the number of visible and subvisible (micrometer-sized) particles (USP <790> and <788>, respectively) in injectable drug products [13,14]. The current pharmacopeial methods include visual inspection and light obscuration or microscopic particle count test for visible and subvisible particles, respectively. Visual inspection may not consistently and reliably detect visible particles in CBMPs because these products may be highly opalescent and viscous due to the high cell concentration (e.g., 10^5-10^7 cells/mL). Furthermore, CBMPs are often supplied as a single-dose, low-volume (microliter to milliliter range) sterile suspension in a (cryo)vial, which has a relatively thick wall, making visual inspection difficult. In addition, subvisible particle analysis by light obscuration is challenging because light obscuration cannot differentiate cells from foreign and particulate impurities. Despite the preceding considerations, from a quality, safety and potentially efficacy perspective, it is prudent that subvisible particles in CBMPs are adequately tested [15].

Flow imaging microscopy (FIM) techniques have been widely used for the characterization of subvisible particles in protein-based drugs [16]. Using these techniques, one can derive concentration, size and morphological parameters of particles within the micrometer size range from microscopic images. Different particle populations can be discriminated based on particle structure and appearance [17,18]. Recently, FIM has been applied to study cell viability and confluency in cell culture as well as quality of CBMPs [12,19-21]. However, comprehensive particle characterization reaches a limit when using the morphological parameters derived from the instruments' operating software because of the complexity of CBMPs, which may consist of multiple particulate populations of highly heterogeneous morphologies.

Deep learning for image analysis is an alternative approach, offering more insight into the collected data and potentially allowing for a better discrimination of particle populations. The increasing computing power and advancements in algorithms for pattern recognition have made the deep learning methods, such as convolutional neural networks (CNN), useful tools in many fields, including the biopharmaceutical industry [22]. Deep learning refers to a multilayered neural network consisting of hidden layers as well as an input and output layer. It can be exceptionally effective in extracting intricate structures in raw (pre-processed) data and recognition of representative features that allow categorization of images with minimum error [23]. For example, protein aggregates formed upon different stress methods were imaged by using FIM and successfully discriminated with the aid of CNN, based on the distinct particle morphology resulting from each stress method [24]. In the area of cell biology, CNN have brought microscopy to a new level, where features such as the type of intracellular structures or the cell cycle and type of cells, previously requiring immunohistochemistry, can now be recognized without fluorescent labeling [25].

In our study, we used a flow imaging microscope, FlowCam, to collect images of subvisible particulate matter in T-cell samples and developed an automated image classification method based on CNN for the analysis of the raw images (henceforth referred to as FlowCam-CNN). As a model system, we used suspensions of Jurkat cells (8−16 μm in diameter) and CD3/CD28 Dynabeads (4.5 μm in diameter); the latter are commonly used for T-cell activation and purification. We show that the developed FlowCam-CNN method enables the detection, quantification and characterization of process-related particulate impurities (e.g., Dynabeads, cell-bead adducts) as well as product-related particulates (e.g., cells, cell agglomerates and debris).

Materials and Methods

Materials

T-cell leukemia cells (Jurkat, Clone E6-1, ATCC® TIB152™) were provided by Leiden University Medical Centre (LUMC) as frozen 1-mL aliquots at a total cell concentration of 10^7 cells/mL, and were stored at −140°C in the freezer before use. The Jurkat cells were formulated in high-glucose RPMI 1640 (RPMI medium; ThermoFisher, Waltham, MA, USA) supplemented with 10% fetal bovine serum (FBS; Life Technologies, Eugene, OR, USA) and 10% dimethyl sulfoxide (DMSO) (Life Technologies). Dynabeads Human T-Activator CD3/CD28 for T Cell Expansion and Activation, and low-protein-binding collection tubes were purchased from ThermoFisher. Sterile 5-mL Eppendorf tubes were purchased from VWR (Ismaning, Germany).

Sample preparation

Jurkat cells used in this study as model T cells were thawed and freshly prepared in RPMI medium before analysis. Frozen cell aliquots were thawed at 36°C and resuspended in ~40 mL of RPMI medium. To remove residual FBS and DMSO, the cell suspension was centrifuged at 300 rcf for 10 min at 20°C. The supernatant was removed, and the pellet was resuspended in 10 mL of RPMI medium, unless otherwise stated. The mean concentration of (live and dead) cells was 477 188 ± 85 914/mL with a mean viability of 81% ± 9% (n = 8) as determined by hemocytometry (described subsequently), unless otherwise stated. Cell-containing samples were measured up to 4 h post-thawing, during which the cell viability was not affected (data not shown).

Dynabeads were diluted to an intermediate stock concentration of 10^6 beads/mL (based on the dilution factor of the nominal Dynabead concentration) in RPMI medium and stored at 2−8°C for up to 1 month. The required volume of the intermediate stock was added to cell samples to reach the desired Dynabead concentrations. Reference concentration of Dynabeads stated in the Results section is the expected concentration of Dynabeads in the sample derived from dilution calculations and the original bead concentration stated by the manufacturer. It must be noted that the manufacturer does not use FlowCam for quantification of Dynabeads; therefore, a systematic deviation between reference concentrations and measured concentrations should be anticipated.

Hemocytometry

Cell viability and total cell concentration were determined by using a Bright-Line hemocytometer glass (Merck, Darmstadt, Germany) and an Axiostar Plus microscope (Zeiss, Jena, Germany) with 10 × magnification (Zeiss). The washed cell suspension was diluted twofold with a sterile-filtered 0.4% Trypan Blue solution (Merck, Darmstadt, Germany). Next, 10 μL of the mixture was placed in the hemocytometer and at least 100 cells were counted (both viable−not stained, and nonviable−stained cells), following the manufacturer's recommendations.

Flow imaging microscopy

For characterization of micron-sized particles, a FlowCam 8100 (Fluid Imaging Technologies, Scarborough, ME, USA) equipped with an 80-μm flow cell and a 10 × objective was used. The instrument

was operated by using a VisualSpreadsheet software (v4.10.8). Analysis was performed by using a flowrate of 0.18 mL/min, and the detection thresholds were set to 17 for dark pixels and 15 for light pixels. Images were taken with a high-resolution CMOS camera (1920 × 1200 pixels) at 27 frames/s. In total, a sample volume of 0.5 mL was analyzed with an efficiency of approximately 70% (i.e., the measured sample volume was ~0.35 mL). Cleaning steps between sample measurements involved thorough flushing of the flow cell with 2% Hellmanex III and highly purified water. Diameters are reported as equivalent spherical diameter (ESD), and filters were not applied for imaging pre-processing. Samples were measured in triplicate or sextuplicate unless otherwise stated.

Samples measured within this study contained particles of five distinct populations: single cells, doublet cells, Dynabeads, adducts (defined as a combination of at least one bead with at least one cell) and debris (any other cellular and non-cellular types of particles). For reporting the total determined concentration of cells, we summed the counts of single cells, adducts and 2 × doublet cells. The determined concentration of Dynabeads in measured samples was derived from the summed counts of Dynabeads and adducts.

Generation of particle images for population discrimination

Establishment of threshold values and training of the CNN was performed on manually selected images (4000−4500) of each population class, which was shown to be sufficient for training our model

to a reach high classification accuracy (>0.99). To facilitate the selection process for debris and adducts, samples with elevated numbers of the respective particles were generated prior to FlowCam analysis. Samples enriched in particles representing debris were obtained by submitting freshly resuspended (cryoprotectant free) cell suspensions to two freeze-thaw cycles (-140−36°C). Samples with high numbers of adducts were generated by incubation of cells (~500 000 cells/mL) in presence of Dynabeads in a number ratio of 1:1 for 1.5 h at 37°C and 5% CO_2.

Development of morphological filters for FlowCam

The VisualSpreadsheet software of the FlowCam system outputs 30 morphological parameters for each detected particle within the measured sample. Five of these available parameters—intensity, sigma intensity, convexity, compactness and aspect ratio—were found to have the highest resolving power for particle populations. Values of particle properties for each population class were further clustered into 1-μm sized bins and are presented in box plots (Figure 1). For the development of threshold values used to assign each particle to its class, a similar approach as previously reported for the discrimination of silicone oil and protein aggregate particles was used [17]. Briefly, a stepwise approach was followed, as described in the following paragraphs.

First, Dynabeads and adducts were separated from cells (singlets and doublets) and debris, based on mean particle intensity values.
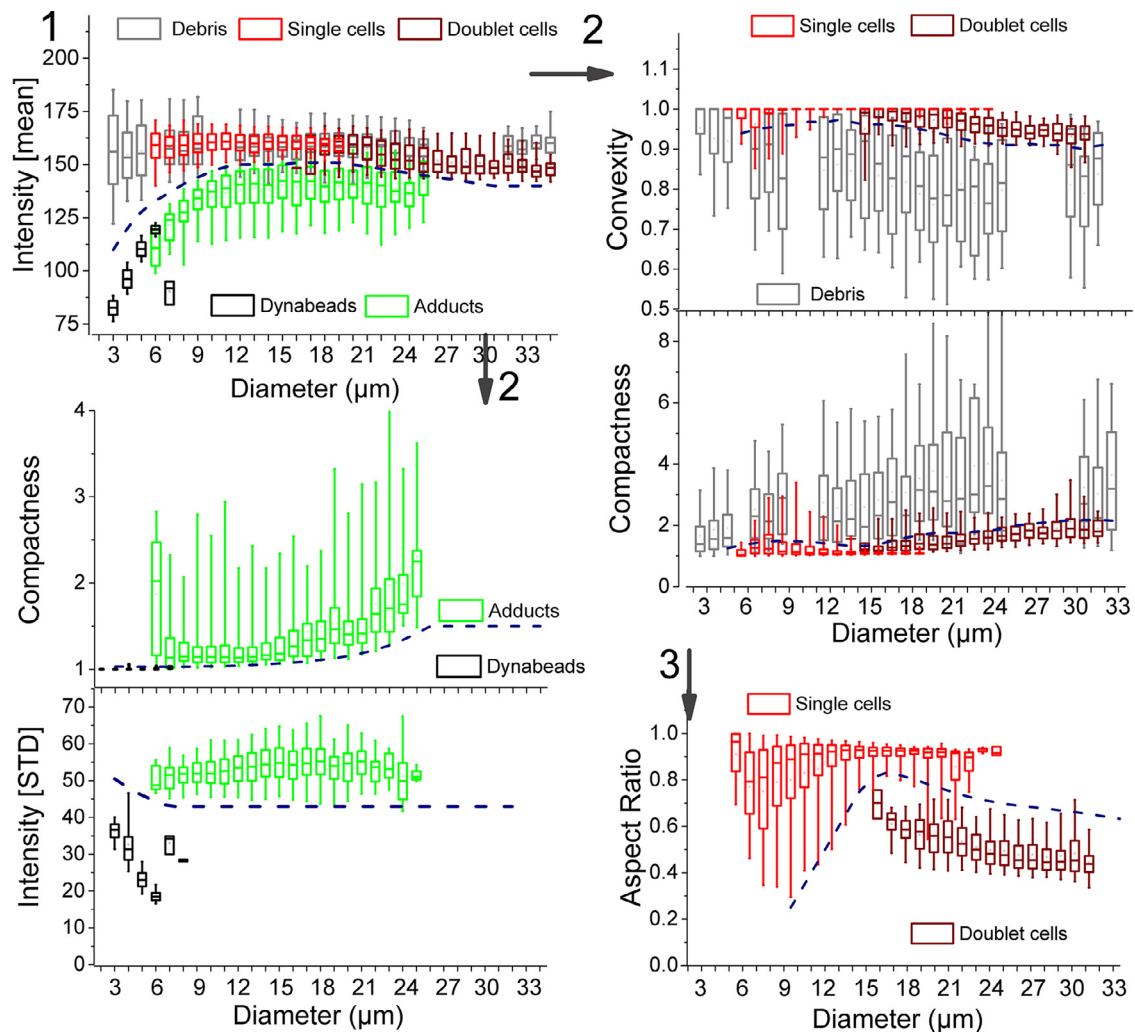

Figure 1. Clustered morphological parameters used to discriminate the five particle populations (see text) by using the output data from the FlowCam software. Arrows with accompanying numbers show the order in which the separation of particle populations was carried out.

For each size bin of 1 μm, average values of the 10th quartile of "low-transparent" particles (Dynabeads and adducts) and of the 90th quartile of "highly transparent" particles (cells and debris) were calculated as a function of size. For size regions in which only one population was present, the cutoff threshold was adjusted manually below or above of the 95th quartile parameter value. Furthermore, a 4-degree polynomial function was fitted to these points from 3 to 35 μm and tested particles of a certain diameter falling above or below the threshold value set were assigned to either group.

Second, threshold values for compactness, convexity and sigma intensity were derived in a similar manner, which allowed for separation of adducts from Dynabeads and cells from debris. For separation of single cells and doublet cells, the aspect ratio parameter was applied. Therefore, each tested particle must have fulfilled at least three criteria to be assigned to a specific population class. All particles with a diameter below 3 μm were assigned to the debris population.

Deep convolutional neural networks

The VGG-19 architecture was used as the foundation for our CNN [26]. This architecture includes 19 convolutional (weight) layers and can capture a large range of visual object features. The network weights are optimized by reformulating convolutional layers as learning residual functions, taking the input to layers as reference. The VGG-19 network used in our studies has been pre-trained on the open source ImageNet dataset found in [27]. By fine-tuning only the last two fully connected layers, the feature complexity of the pre-trained model can be optimized for the particle classification task. For fine-tuning the image dataset was split into test, validation and training sets at a 0.8, 0.1 and 0.1 ratio, respectively. Such division of the dataset was aimed to maintain the classes balanced and so the fine-tuning would not be biased toward a specific class. The deep learning model was fine-tuned with 30 epochs with the Adam optimization algorithm. The machine learning model was implemented in the Keras (2.2.4)-Tensorflow (1.13.1) Python (3.7.3) library and ran on a Nvidia Turing GPU with 11 GB of VRAM. A simplistic workflow for image analysis by using CNN is presented in Figure 2.

Data analysis

Statistical analysis of data was performed in Origin 2016 (Origin-Lab Corporation, Northampton, MA, USA). Box plots represent the distribution of data where central rectangles span from the first to the third quartile and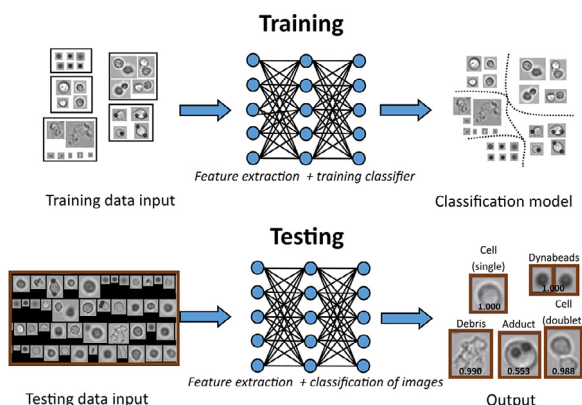 whiskers range from the 5th up to the 95th percentile values. For comparison of mean values, a two-sided Student's t-test with α = 0.05 (95% confidence interval) was used.

The limit of detection (LOD) and limit of quantification (LOQ) were determined by using values of the entire tested range for Dynabeads, where six measurement replicates were performed for each bead concentration. LOD and LOQ were calculated by using Eqs. 1 and 2 [28]:

$$LOD = (3.3 * \sigma)/S \qquad (1)$$

$$LOQ = (10 * \sigma)/S \qquad (2)$$

where σ is the standard error of the y-intercept, and S is the slope of the linear regression line.

Results

Identification of particle populations in cell suspensions

Analysis of cell suspensions supplemented with Dynabeads was performed by using FlowCam and representative examples of generated images of the five distinct particle populations are shown in Figure 3. Besides single cells, debris and Dynabeads, we observed a noticeable number of images with two captured cells (doublet cells) as well as cells with one or more adjacent Dynabeads (adducts). Particle size distributions of samples containing cells (without beads), Dynabeads (without cells) and a mixture of cells and Dynabeads are shown in Figure 3. Samples containing cells showed a broad peak between 10 and 16 μm, representing the Jurkat cells (Figure 3A). Furthermore, a sharp peak at the lower size limit of detection was observed and assigned to debris. Dynabeads showed a bimodal peak with maxima at 3.5 and 6.0 μm (Figure 3B). These values represent the measured size of beads from in-focus (sharp) and out-of-focus (blurred) images and are close to the mean bead diameter of 4.5 μm stated by the manufacturer. Particle size distributions of mixtures of Dynabeads and cells looked like a summation of the cells and the beads (Figure 3C). Although these samples were found to contain adducts (see Figure 3, top panel), which obviously were not present in the other samples, the number of adducts was relatively small and did not substantially affect the overall size distribution.

Morphological parameters for particle classification

For beads suspended in the RPMI medium, a linear relation was found between the measured Dynabead concentration and the expected Dynabead concentration derived from the dilution factor, with a linearity of R^2 = 0.95 (supplementary Figure 1A), based on the selected morphological parameters with the FlowCam software (cf. Figure 1). Measurements of beads in the presence of cells (~500 000 total cells/mL by using a hemocytometer) resulted in a similar linear correlation (R^2 = 0.98). However, unexpectedly high numbers of unclassified particles (i.e., particles with morphological parameters not falling into any of the five classes) were found. The coefficient of variation for measured concentrations of Dynabeads in presence of cells was noticeably higher compared with the control samples. Additionally, the recovery of Dynabeads in cell suspensions at the lowest three reference concentrations was >100%, suggesting a number of debris and other particles were misclassified as Dynabeads (or adducts) when using this approach. Dynabeads suspended in RPMI medium showed recovery rates from 25% (lowest Dynabead concentration) up to 85% (highest Dynabead concentration) (data not shown). Altogether, using the morphological particle parameters output from the FlowCam software resulted in a good correlation between detected concentrations and reference concentrations of Dynabeads. However, the high numbers of unclassified particles and the noticeable variation in determined particle concentrations illustrate the friability of this classification approach.
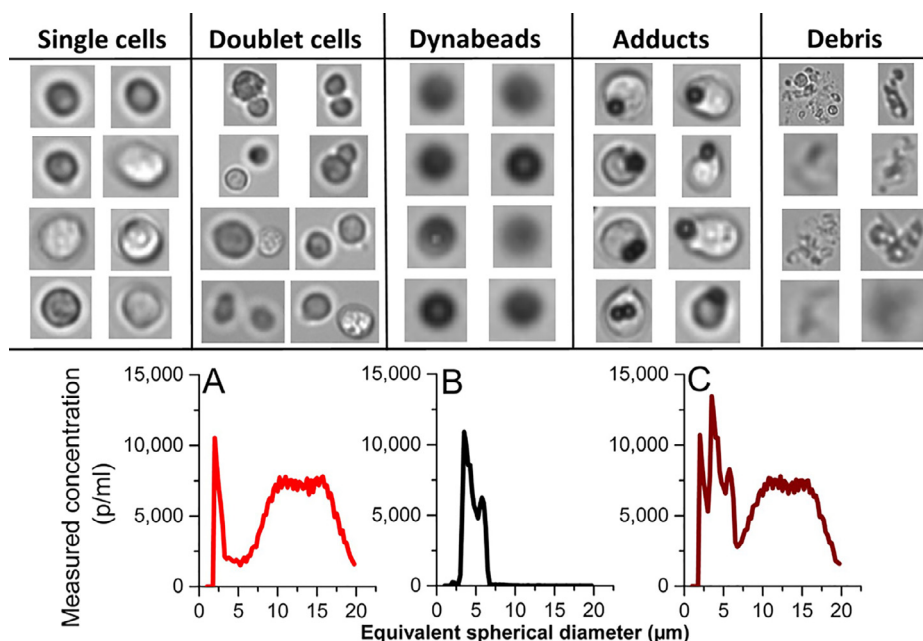

Training

Feature extraction + training classifier

Training data input   Classification model

Testing

Feature extraction + classification of images

Testing data input

Output

Cell (single)   Dynabeads
1.000   1.000
Debris   Adduct   Cell (doublet)
0.990   0.553   0.988

Figure 2. Illustration of the CNN work flow. First, a collection of 4000−4500 images from each particle class was manually selected for training with the VGG-19 network. During training, kernels of weights in the two last layers of our network are updating weight parameters and extracting representative image descriptors based on the input data. Once training is completed, the network can be used to predict particle classes of new (not used during training) images. Output is given as a probability of an image assigned to the stated class. A detailed description of the VGG-19 network can be found in Simonyan et al. [26].

Figure 3. Representative images of each population class obtained by using FlowCam (top). All images were enlarged for presentation and actual size is not represented. Particle size distributions of samples containing (A) Jurkat cells (375 000 cells/mL), (B) Dynabeads (68 000 beads/mL) and (C) Jurkat cells + Dynabeads (bottom).

CNN for particle classification

Because accurate discrimination of particle populations, present in cell suspensions, was not satisfactory with conventional morphological filters, we applied CNN for analysis of raw FlowCam images. The fine-tuned FlowCam-CNN model with the pre-selected datasets (see methods section above and Figure 2) was used to classify on average 140 000 images per sample into individual particle classes.

Detection and quantification of Dynabeads

In contrast to the results based on the morphological particle parameters output described above, FlowCam-CNN analysis resulted in classification of all particles present cell suspensions (500 000 cell/mL counted by using a hemocytometer) with or without Dynabeads (Figure 4). Linearity over the entire tested Dynabead concentration range was >0.95 for both sample sets, and slope values were ~0.8. Samples containing cells and >50 000 beads/mL had recovery values >80% and a coefficient of variation below 15%. The relative error of the determined bead concentration was apparently random and showed a uniform distribution around 0 for samples with cells, except for the lowest bead concentrations measured (data not shown). Dynabeads suspended in cell-free RPMI medium at reference concentrations <60 000 beads/mL showed lower recoveries compared with samples containing cells, which exceeded a recovery rate of 75% within the tested range. The coefficient of variation of determined Dynabead concentrations was >10% for samples with <50 000 beads/mL and <10% for the higher tested bead concentrations. Therefore, the optimal Dynabead concentration for quantification of beads by using FlowCam-CNN was determined to be from ~45 000 beads/mL to at least 200 000 beads/mL.

The FlowCam method assisted with automated image classification (FlowCam-CNN) was examined in alignment with the ICH Q2 (R1) guideline for validation of analytical procedures. Accuracy, precision, LOD, LOQ and linear relationship for Dynabeads detection in absence and presence of cells were evaluated and the results are presented in Table I.

The LOD and LOQ were ~15 000 and 45 000 beads/mL, respectively, whereas slightly higher values were found for Dynabead suspensions in absence of cells.

Accuracy and precision (repeatability) were calculated for Dynabead concentrations above the LOQ, and the values present averages of two intra-day sets of triplicate measurements. Accuracy was determined as the recovery of spiked in Dynabeads with respect to the reference concentrations (Recovery%). Accuracy was found to be substantially lower for beads in absence of cells at reference concentrations <50 000 beads/mL. Above this concentration, the presence of cells did not have an impact on the accuracy of quantification. Furthermore, precision of Dynabeads concentration determination was evaluated as the coefficient of variation (CV%) and overall values were <10%.

Characterization of cellular particulate matter

In addition to developing a method for characterization of non-cellular particles, we aimed to quantify debris (a potential impurity) as well as cells and adducts.

The tested concentrations of Dynabeads in Jurkat cell suspensions, presented in Figure 4, were studied at a constant cell concentration (385 711 ± 59 337 cells/mL as determined with FlowCam). The presence of Dynabeads did not have a significant impact on the number of quantified total number of cells (*t*-test, two-sided, $P > 0.17$; supplementary Figure 2A). Moreover, the numbers of detected particles classified as debris in cell samples without and with Dynabeads were highly comparable. Furthermore, as expected, the number of detected adducts increased with higher concentrations of beads present in cell samples (supplementary Figure 2B,C).

Misclassifications

The misclassification rate was calculated in an indirect manner because of the large number of acquired images per measurement (>100 000 per measurement). Debris particles were present in all measured samples (Dynabeads and cell suspensions); therefore, we did not consider the misclassification rate for this population. Figure 5A represents the rates of erroneously detected cells (singlets, doublets and adducts) and of unclassified particles within Dynabead suspensions of different reference concentrations. Figure 5B presents the error rates of detected Dynabeads and adducts as well as unclassified particles within cell only suspensions at a cell concentration of ~375 000 cells/mL (as measured by FlowCam). In both cases, the
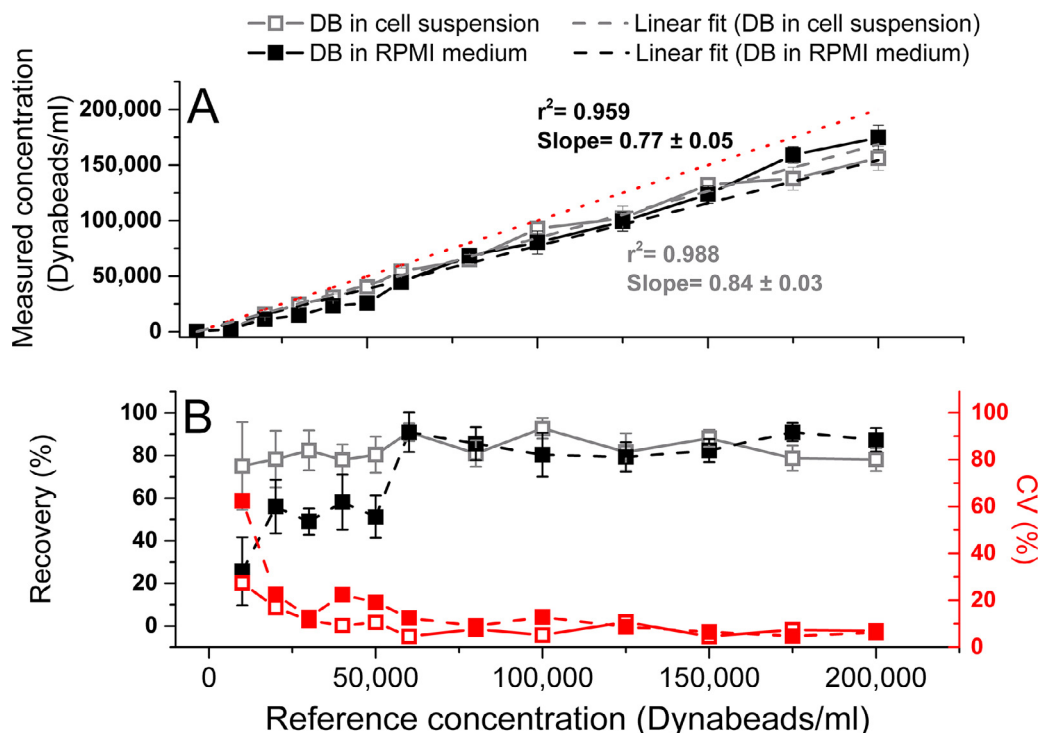
Figure 4. Presented data on classified Dynabeads (DB) by using CNN. (A) Determined concentration of Dynabeads in a concentration series of Dynabeads suspended in RPMI medium (DB ctrl, gray) and in Jurkat cell suspensions (DB + cells, black). (B) Recovery (left y-axis, black) and corresponding coefficient of variation (CV; right y-axis, red) of Dynabeads in RPMI medium (open squares) and Jurkat cell suspensions (closed squares). Error bars represent the standard deviation of mean values of six replicates. The coefficient of variation values (%) were calculated from the six replicate measurements.

Table I
Parameters determined by FlowCam-CNN based on mean values of two inter-day triplicate measurements.

Parameter	Dynabeads (in cell suspension)	Dynabeads (in RPMI 1640 medium)
Accuracy (Recovery%)	86.9 ± 5.4	80.5 ± 12.6
Precision (CV%)	4.7 ± 0.9	8.0 ± 3.2
LOD (beads/mL)	15 229	13 661
LOQ (beads/mL)	46 149	41 396
Linearity (R^2)	0.988	0.959

The LOD and LOQ were deteremined for Dynabead concentrations tested in the study and presented in Figure 4. Accuracy and precision were determined for Dynabead concentrations above the LOQ. Cell concentration was ~375 000 cells/mL.

misclassification rates were very low (<2%) when the data was processed by using CNN. Furthermore, the error rate was independent of the spiked-in amount of Dynabeads, as the fraction of misclassified particles was similar for each of the tested concentration of beads in cell suspensions. Particles analyzed by using morphological parameters showed a much higher inaccuracy and unclassified fraction, which is reflected by the relatively high error rates (up to 50-fold higher compared to CNN).

Figure 6 presents the probability distribution, as determined by deep learning classification, of particle images classified as Dynabeads. Particle images were collected during FlowCam measurements of Dynabeads (80 000 beads/mL) in presence and absence of cells. In our classification network, the Softmax regression function was integrated, which is an activation function converting calculated weights
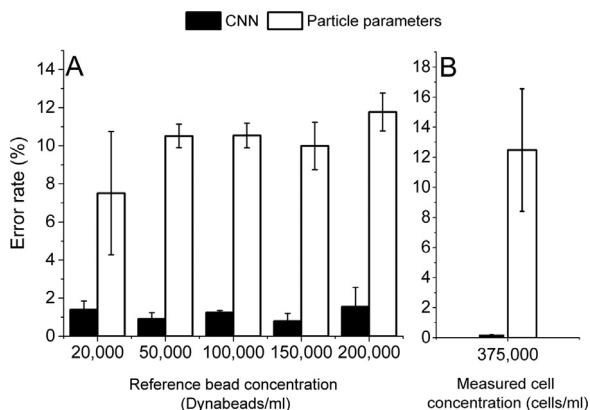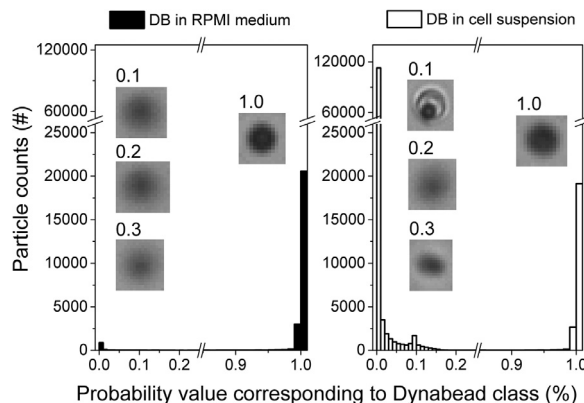

Figure 5. Error rates of particles classified as (A) cells or adducts in Dynabead suspensions with different Dynabead target concentrations (x-axis) and (B) Dynabeads and adducts in cell suspensions at 375 000 cells/mL (as determined by using FlowCam). Error rates are based on misclassified particles by using CNN (filled bars), and on misclassified and unclassified particles by using particle morphological parameters (empty bars). Error bars are standard deviations of mean values of six replicates.

Figure 6. Probability distribution (binned in units of 0.01) of classified particle images determined by FlowCam-CNN for Dynabead suspension (filled) and cell suspension suplemented with Dynabeads (empty) at a concentration of 80 000 beads/mL. Representative images are shown with their asssgned probability of belonging to the Dynabead class.

into probability distributions and rejecting all cases with probabilities <0.2. For the sample with suspended Dynabeads in RPMI medium, the vast majority of images classified to the bead class had a probability equal to 1, which confirmed that the network made the assignment with very high confidence. Moreover, this high confidence was not impacted by the presence of cellular material in the sample, as similar counts of beads with a probability of 1 were found in samples containing Jurkat cells. In conclusion, these data demonstrate that image classification by using FlowCam-CNN is highly accurate.

Effect of cell concentration on measurement

The impact of the Jurkat cell concentration on the quantification of Dynabeads in cell suspensions by FlowCam-CNN was investigated, and the results are presented in Figure 7. Dynabeads spiked into samples with cell concentrations up to ~500 000 cells/mL (as determined by using a hemocytometer) resulted in similar measured bead concentrations in presence of cells. At the highest tested cell concentration (900 000 cells/mL), we observed an underestimation of detected beads at reference Dynabead concentrations of 50 000 and 100 000 beads/mL. Such an underestimation was not observed for the lowest tested Dynabead concentration (20 000 beads/mL). Furthermore, control samples showed lower Dynabead recoveries compared with samples with cell suspensions.

Discussion

Characterization of cellular and non-cellular (i.e., foreign) particulate matter in CBMPs is important to guarantee a good quality and safe product [8]. Additionally, with the limited time available for analytical testing of some cell products, straightforward, rapid and comprehensive methods are urgently needed [5].

In this study we used a model system containing Jurkat cells, serving as a surrogate for T cells, such as CAR-T cells [29], and Dynabeads CD3/CD28, serving as a representative potential process-related particulate impurity in CAR-T cell products [30]. These super-paramagnetic beads coupled to CD3 and CD28 monoclonal antibodies are used in the production of CBMPs [31]. However, their removal before the final formulation step remains difficult [32]. More important,

taking into consideration reports on the potential toxicity of Dynabeads [30], methods showing effective and consistent removal of these impurities in the manufacturing process are required. Therefore, in our study, we assessed the feasibility of FIM for the discrimination of Dynabeads and cells, and for the assessment of the Dynabead concentration. We hypothesized this should be possible because Dynabeads differ in size and morphological properties from T cells. It must be noted that the full production protocol, where beads are present in cell medium for days or weeks, was not mimicked here; Dynabeads were spiked into cell suspensions shortly before analysis. Therefore, monitoring the stability of beads in the suspension and their interactions with cells over time was beyond the scope of this study.

The FIM-based method may offer advantages for characterizing CBMPs because it is a high-throughput technique capable of rapid measurements of high sample numbers without laborious preparative steps. The two most commonly used FIM systems are FlowCam and Micro-Flow Imaging (MFI). Previously, it has been shown that FIM techniques have the potential in determination of cell concentration and viability [12]. For our study, FlowCam was chosen because of its capability of recording images of high quality and its high accuracy and precision in particle concentration determination [33]. A downside of the FlowCam technique can be the relatively inaccurate particle sizing, resulting from a narrow depth of focus within the field of the imaging system. As a result, particles of a homogenous diameter may show a bimodal distribution [34], which was also observed in the present study (Figure 3). Accurate sizing was not of key importance in our study. However, in-focus and out-of-focus images should both be assigned to the same particle class, implying an increase in complexity of the classification process.

The verification of viability and total concentration of cells used in our study was performed by using a hemocytometer. As shown in previous studies [12,21], cell concentrations determined by using FlowCam were lower compared with manual counting, and in our case the difference was ~20%. Furthermore, the concentration of Dynabeads detected by FlowCam deviated from the reference concentrations stated by the manufacturer, that is, the recovery was always <100% especially for Dynabeads at lower concentrations. This, however, can most likely be ascribed to a loss of beads during
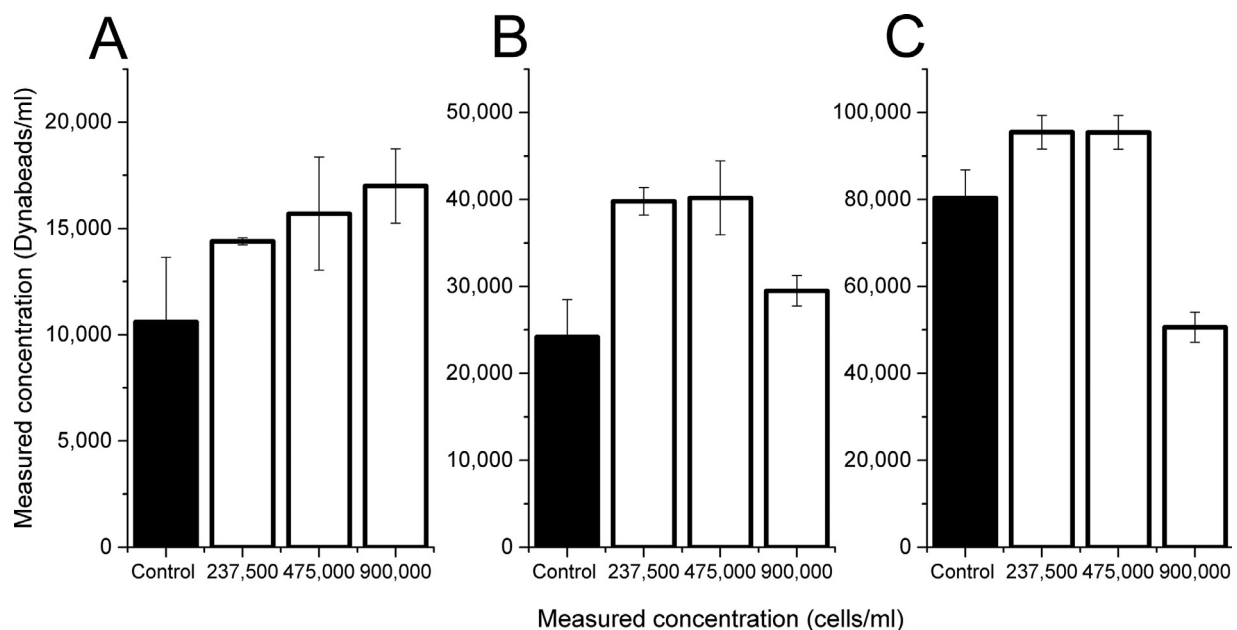

Figure 7. Determined concentration of Dynabeads in RPMI medium (control; filled bars) and cell suspensions (empty bars). Three different cell concentrations (x- axis; determined by using hemocytometry) were tested with reference concentrations of Dynabeads of (A) 20 000, (B) 50 000 and (C) 100 000 Dynabeads/mL. Error bars represent standard deviations of triplicate measurements of Dynabeads in cell suspensions and of nonuplet measurements of Dynabeads in RPMI medium.

sample preparation, as measurements with a Multisizer 4e Coulter-Counter analyzer (method used by the manufacturer for quantification) showed similar results (data not shown). Moreover, preliminary studies showed a significant impact of used lab disposables (e.g., low-protein binding materials, volume-to-surface ratios) on the determined concentration of Dynabeads. The high affinity of the antibody coated beads to surfaces resulted most probably to adherence of Dynabeads to polypropylene tubes and tips used for sample handling. Interestingly, a more consistent and higher recovery rate was observed for Dynabeads in presence of cells compared to Dynabeads in cell-free RPMI buffer (control) over the measured concentration range. In particular, a pronounced loss of beads at low concentrations (<60 000 beads/mL) was observed in our cell-free control samples, resulting in a recovery below 50%. Such high losses of Dynabeads were not observed in the cell-containing samples, in which most likely debris and other cell-related materials occupied free surfaces and competitively decreased bead adsorption. Because the bead-to-T-cell ratio is critical for T-cell activation or purificiation [35], bead-preparative steps where dilutions in cell-free media are involved should be carefully considered to reach the desired bead concentration and assure a consistent manufacturing process.

When using FIM, a capable demarcation approach is required for accurate quantification of specific particle populations found within highly heterogeneous samples. Output parameters by the instruments' operating software can be helpful in discriminating particles based on morphology but may be prone to high error rates [18]. The uniformity of Dynabead images resulted in similar values of each particle parameter and developed filters had close to no misclassifications and 5% of unclassified particles for Dynabead-only samples. However, the morphological nature of cells, cell aggregates and debris is highly heterogeneous and the distribution of each of these particle parameters was highly disperse (Figure 1). Furthermore, adducts and cells had in many cases interchangeable values for most particle parameters. The error rates (misclassifications and unclassified particles) for images containing only cells were approximately 20% with datasets used for developing morphological filters. Error rates for cell and Dynabead suspensions were ~10% with testing datasets. The lack of a high capability in discrimination of different particle population groups by using morphological parameters prompted us to use an automated image classification method based on CNN.

Compared with other machine learning techniques, deep learning is straightforward to use and achieves high accuracies with minimal refinements to the network layers [22]. The high performance of neural networks is in most cases based on large datasets to train the networks. For successful training of an entire CNN, such as VGG-19, several million labeled images per class are required. Although FIM techniques are well suited for applications where comparably large numbers of images can be collected within a relatively short period of time and with low sample consumption, cleaning and labeling a high-quality training dataset remains a challenge. Because the pre-trained VGG-19 was able to efficiently differentiate features on the ImageNet dataset, fine-tuning of the last two fully connected layers by using a relatively small number of labeled FlowCam images resulted in a powerful CNN for differentiation and quantification of Dynabeads. The misclassification rate was significantly reduced with the CNN and was only 0.2% for cell samples spiked with Dynabeads. FlowCam-CNN was capable of quantifying a wide concentration range of Dynabeads in cell suspensions, demonstrating a large dynamic range. Furthermore, the high precision (CV% < 5%) in determination of Dynabead concentration in cell suspensions above the LOQ presents this method as a robust approach for quantification of process-related particulates.

The determined total cell and debris concentration was not affected by the number of Dynabeads spiked into the suspension (supplementary Figure 2). As expected, the number of detected adducts increased with increasing concentration of Dynabeads in the sample because of the higher probability of beads interacting with cells. Furthermore, a concentration of 500 000 cells/mL showed to have no impact on the quantification of Dynabeads in cell suspensions. However, at the highest cell concentration tested, we observed a clear decrease in recovery of Dynabeads, which were spiked to a target concentration 50 000 and 100 000 beads/mL. This loss in recovery was not observed for the lowest Dynabead concentration of 20 000 beads/ml. A possible explanation could be the approach for counting Dynabead(s) attached to a single cell. Cases in which a particle was classified as "adduct" were considered to consist of a single cell and a single Dynabead, which was true in the majority of cases. However, with increasing number of cells or Dynabeads, the probability of capturing a cell with two or more adhering Dynabeads per image becomes higher. Therefore, the underestimation of Dynabeads could have been related to the inaccurate counting of beads in dense cell populations.

Conclusions and Outlook

In our study, we developed a reliable method based on FIM coupled with CNN for detection, characterization and quantification of relevant particulate impurities, specifically Dynabeads. We showed that small amounts of Dynabeads can be detected in cell suspensions and a high precision in counting is achieved if the bead concentration is above the determined LOQ. Moreover, cells and cellular impurities, such as cell aggregates and adducts, can be easily classified by using CNN. Quantification of these particles can assist in monitoring manufacturing processes of CBMPs and assist in process and product characterization, such as stability testing.

Further work is being carried out to enhance the capabilities of the method for other cell lines, the identification of multiple beads adhering to cells, as well as to characterize other populations of particulates potentially present in CBMPs, such as leachables, extractables and beads used as carriers for the *ex vivo* expansion of adherent cells. In addition, further evaluation of the presented method by using orthogonal methods could endorse the results obtained from the currently opaque processing algorithm, such as CNN [36]. This would increase confidence and understanding of FlowCam-CNN, presumably supporting in-process and QC analyses at first, and potentially becoming a critical release test. Currently, we are not aware of other methods with similar performance and we believe that CBMP development can benefit from FlowCam-CNN in its current state.

Funding

Declaration of Competing Interest

The authors have no commercial, proprietary, or financial interest in the products or companies described in this article.

Author Contributions

Conception and design of the study: AG, TM, KH, KP, AH and WJ. Acquisition of data: AG and ES. Analysis and interpretation of data: AG, ES, TM, AH, and WJ. Drafting or revising the manuscript: AG, TM, KH, KP, AH and WJ. All authors have approved the final article.

Supplementary materials

Supplementary material associated with this article can be found in the online version at doi:10.1016/j.jcyt.2020.04.093.

References

[1] La G de Torre B, Albericio F. The pharmaceutical industry in 2018. an analysis of FDA drug approvals from the perspective of molecules. Molecules 2019;24(4). https://doi.org/10.3390/molecules24040809.

[2] Roh K-H, Nerem RM, Roy K. Biomanufacturing of therapeutic cells: state of the art, current challenges, and future perspectives. Annu Rev Chem Biomol Eng 2016;7:455–78. https://doi.org/10.1146/annurev-chembioeng-080615-033559.

[3] Holzinger A, Abken H. Advances and challenges of CAR T cells in clinical trials editor. In: Theobald M, ed. current immunotherapeutic strategies in cancer, Cham: Springer International; 2020:93–128.

[4] Jönsson B, Hampson G, Michaels J, Towse A, von der Schulenburg J-MG, Wong O. Advanced therapy medicinal products and health technology assessment principles and practices for value-based and sustainable healthcare. Eur J Health Econ 2019;20(3):427–38. https://doi.org/10.1007/s10198-018-1007-x.

[5] Kaiser AD, Assenmacher M, Schröder B, et al. Towards a commercial process for the manufacture of genetically modified T cells for therapy. Cancer Gene Ther. 2015;22(2):72–8. https://doi.org/10.1038/cgt.2014.78.

[6] European Medicines Agency. Guideline on quality, non-clinical and clinical aspects of medicinal products containing genetically modified cells. 2018. https://www.ema.europa.eu/en/documents/scientific-guideline/draft-guideline-quality-non-clinical-clinical-aspects-medicinal-products-containing-genetically_en.pdf. Accessed 1.12.2019.

[7] Rosenberg G. Microscopic haematology:a practical guide for the laboratory. Amsterdam: Harwood Academic 1997.

[8] Clarke D, Stanton J, Powers D, et al. Managing particulates in cell therapy: Guidance for best practice. Cytotherapy 2016;18:1063–76. https://doi.org/10.1016/j.jcyt.2016.05.011.

[9] Narhi LO, Corvari V, Ripple DC, et al. Subvisible (2-100 μm) Particle analysis during biotherapeutic drug product development: part 1, considerations and strategy. J Pharm Sci 2015;104(6):1899–908. https://doi.org/10.1002/jps.24437.

[10] Jiskoot W, Kijanka G, Randolph TW, et al. Mouse models for assessing protein immunogenicity: lessons and challenges. J Pharm Sci 2016;105(5):1567–75. https://doi.org/10.1016/j.xphs.2016.02.031.

[11] Moussa EM, Panchal JP, Moorthy BS, et al. Immunogenicity of therapeutic protein aggregates. J Pharm Sci 2016;105(2):417–30. https://doi.org/10.1016/j.xphs.2015.11.002.

[12] Sediq AS, Klem R, Nejadnik MR, Meij P, Jiskoot W. Label-free, flow-imaging methods for determination of cell concentration and viability. Pharm Res 2018;35 (8):150. https://doi.org/10.1007/s11095-018-2422-5.

[13] General Chapter. <788>Particulate matter in injections. The United States Pharmacopeial Convention; 2013. p. 350–3.

[14] General Chapter. <790>Visible particulates in injections. The United States Pharmacopeial Convention; 2014. p. 6393–4.

[15] Levine BL, Miskin J, Wonnacott K, Keir C. Global manufacturing of CAR T cell therapy. Mol Ther Methods Clin Dev 2017;4:92–101. https://doi.org/10.1016/j.omtm.2016.12.006.

[16] Corvari V, Narhi LO, Spitznagel TM, et al. Subvisible (2-100 μm) particle analysis during biotherapeutic drug product development: part 2, experience with the application of subvisible particle analysis. Biologicals 2015;43(6):457–73. https://doi.org/10.1016/j.biologicals.2015.07.011.

[17] Weinbuch D, Zölls S, Wiggenhorn M, et al. Micro-flow imaging and resonant mass measurement (Archimedes)—complementary methods to quantitatively differentiate protein particles and silicone oil droplets. J Pharm Sci. 2013;102(7):2152–65. https://doi.org/10.1002/jps.23552.

[18] Akhunzada ZS, Hubert M, Sahin E, Pratt J. Separation, characterization and discriminant analysis of subvisible particles in biologics formulations. Curr Pharm Biotechnol 2019;20(3):232–44. https://doi.org/10.2174/1389201020666190214100840.

[19] Farrell CJ, Cicalese SM, Davis HB, et al. Cell confluency analysis on microcarriers by micro-flow imaging. Cytotechnology. 2016;68(6):2469–78. https://doi.org/10.1007/s10616-016-9967-0.

[20] Wu L, Martin T, Li Y, et al. Cell aggregation in thawed haematopoietic stem cell products visualised using micro-flow imaging. Transfus Med 2012;22(3):218–20. https://doi.org/10.1111/j.1365-3148.2012.01147.x.

[21] Vollrath I, Mathaes R, Sediq AS, et al. Subvisible particulate contamination in cell therapy products-can we distinguish? J Pharm Sci. 2019. https://doi.org/10.1016/j.xphs.2019.09.002.

[22] LeCun Y, Bengio Y, Hinton G. Deep learning. Nature 2015;521:436–44. https://doi.org/10.1038/nature14539.

[23] Schroff F, Kalenichenko D, Philbin J. FaceNet: A unified embedding for face recognition and clustering. Cornell University; 2015. https://doi.org/10.1109/CVPR.2015.7298682.

[24] Calderon CP, Daniels AL, Randolph TW. Deep convolutional neural network analysis of flow imaging microscopy data to classify subvisible particles in protein formulations. J Pharm Sci 2018;107(4):999–1008. https://doi.org/10.1016/j.xphs.2017.12.008.

[25] Christiansen EM, Yang SJ, Ando DM, et al. In silico labeling: predicting fluorescent labels in unlabeled images. Cell. 2018;173(3):792–803.e19. https://doi.org/10.1016/j.cell.2018.03.040.

[26] Simonyan K, Zisserman A. Very deep convolutional networks for large-scale image recognition; 2014. http://arxiv.org/pdf/1409.1556v6. Accessed 01.2.2020.

[27] Russakovsky O, Deng J, Su H, et al. ImageNet large scale visual recognition challenge. Int J Comput Vis. 2015;115(3):211–52. https://doi.org/10.1007/s11263-015-0816-y.

[28] Borman P, Elder D. Q2(R1) Validation of analytical procedures. In: Teasdale A, Elder D, Nims R, eds. ICH quality guidelines: an implementation guide, Wiley Online Books; 2017:127–66.

[29] Baeuerle PA, Ding J, Patel E, et al. Synthetic TRuC receptors engaging the complete T cell receptor for potent anti-tumor response. Nat Commun 2019;10(1):2087. https://doi.org/10.1038/s41467-019-10097-0.

[30] Tiwari A, Punshon G, Kidane A, Hamilton G, Seifalian AM. Magnetic beads (Dynabead) toxicity to endothelial cells at high bead concentration: implication for tissue engineering of vascular prosthesis. Cell Biol Toxicol 2003;19(5):265–72.

[31] Wang X, Rivière I. Clinical manufacturing of CAR T cells: foundation of a promising therapy. Mol Ther Oncolytics 2016;3:16015. https://doi.org/10.1038/mto.2016.15.

[32] Iyer RK, Bowles PA, Kim H, Dulgar-Tulloch A. Industrializing autologous adoptive immunotherapies: manufacturing advances and challenges. Front Med (Lausanne) 2018;5:150. https://doi.org/10.3389/fmed.2018.00150.

[33] Werk T, Volkin DB, Mahler H-C. Effect of solution properties on the counting and sizing of subvisible particle standards as measured by light obscuration and digital imaging methods. Eur J Pharm Sci 2014;53:95–108. https://doi.org/10.1016/j.ejps.2013.12.014.

[34] Zölls S, Weinbuch D, Wiggenhorn M, et al. Flow imaging microscopy for protein particle analysis—a comparative evaluation of four different analytical instruments. AAPS J 2013;15(4):1200–11. https://doi.org/10.1208/s12248-013-9522-2.

[35] Kalamsz D, Long SA, Taniguchi R, Buckner J, Berenson R, Bonyhadi M. Optimization of human T-cell expansion ex vivo using magnetic beads conjugated with Anti-CD3 and Anti-CD28 antibodies. J Immunother 2004(27):405–18. https://doi.org/10.1097/00002371-200409000-00010.

[36] Price WN. Big data and black-box medical algorithms. Sci Transl Med 2018;10 (471). https://doi.org/10.1126/scitranslmed.aao5333.